

A new empirical method of estimation of the far-infrared flux of galaxies

Hirohisa NAGATA, Hiroshi SHIBAI

Graduate School of Science, Nagoya University, Furo-cho, Chikusa-ku, Nagoya, 464-8602

hnagata@u.phys.nagoya-u.ac.jp

Tsutomu T. TAKEUCHI*

National Astronomical Observatory, Mitaka, Tokyo 181-8588

and

Takashi ONAKA

Department of Astronomy, Graduate School of Science, The University of Tokyo, 7-3-1 Hongo,

Bunkyo-ku, Tokyo 113-0033

(Received 2002 February 14; accepted 2002 August 7)

Abstract

We propose a new empirical method to estimate the total far-infrared flux of galaxies from the spectral energy distribution (SED) at wavelengths $\lambda \leq 100 \mu\text{m}$. It is difficult to derive the total far-infrared luminosity from only the IRAS data, though it is one of the most important properties of galaxies. Observations by Infrared Telescope in Space (IRTS) indicate that the SED of the diffuse emission from the Galactic plane in this wavelength region can be derived from the $60 \mu\text{m}$ to $100 \mu\text{m}$ color. This empirical SED relation was improved in order to obtain a better fit to the Galactic plane data for $I_\nu(60 \mu\text{m})/I_\nu(100 \mu\text{m}) > 0.6$, and applied to 96 IRAS galaxies for which ISOPHOT and KAO data are available at $\lambda > 100 \mu\text{m}$. As a result, the empirical relation describes well the far-infrared (FIR) SED for a majority of the galaxies. Additionally, the total FIR flux for $\lambda \geq 40 \mu\text{m}$ is derived from the flux densities at 60 and $100 \mu\text{m}$ by using this model. For the 96 IRAS galaxies, the uncertainty in the total far-infrared flux of the present method is 26 %. The present method is more accurate than the previous one widely used to derive the total infrared flux from the IRAS 60 and $100 \mu\text{m}$ data.

Key words: ISM: dust, extinction—galaxies: ISM—galaxies: spiral

* A Research Fellow of the Japan Society of the Promotion of Science (JSPS).

1. Introduction

In the interstellar space of galaxies, there exist solid particles of sub-micron sizes, so called “interstellar dust grains.” Earlier work (e.g., Beichman 1987; Soifer et al. 1987) has revealed that the far-infrared emission from galaxies is often dominated by thermal emission from such dust grains. Therefore, the total luminosity in the far-infrared from the interstellar dust grains is the most important indicator of star-formation activity or activity of hidden AGNs. Moreover, the far-infrared color is the most direct indicator of the strength of interstellar radiation field (ISRF).

Over the past two decades, many studies have been made to understand the properties of infrared emission from interstellar dust grains. In order to explain the observed spectral energy distribution (SED) of the Galactic plane, Désert et al. (1990) proposed a three-component model that consists of large grains (LGs), very small grains (VSGs), and polycyclic aromatic hydrocarbons (PAHs). The large grain is the classical interstellar dust grain of sub-micron size, which is thought to be in equilibrium with the interstellar radiation field. Bulk of the emission from the large grains is radiated in the far-infrared and sub-millimeter wavelength regions. The very small grain is the dust grain heated transiently up to a few hundred K by the incidence of a single UV photon. A number of dust models (e.g., Draine and Anderson 1985) have shown that both stochastically heated VSGs with radii of less than 10 nm and very large molecules with up to a few hundred atoms could be the source of the excess emission shorter than 100 μm . Dwek et al. (1997) showed that the mean infrared SED of the Galactic plane was fitted with a composite model of silicate and graphite grains. If we take the silicate dust grain to correspond to the large grain, and the graphite to the very small grain, these two models have essentially the same approach to reproduce the observed SED of the Galactic plane.

By using the Infrared Telescope in Space (IRTS) and the Infrared Astronomical Satellite (IRAS) data, Okumura et al. (1999) and Shibai et al. (1999) proposed another approach. They assumed that the SED between 100 and 200 μm is dominated by a single-component dust with an emissivity index of 2 at a nearly constant temperature. They showed that the observed SED can successfully be fitted with the single component model at a constant temperature, which means that the strength of the interstellar radiation field (ISRF) is nearly a constant, except for the high-temperature regions around distinct H II regions. However, the diffuse infrared emission at wavelengths λ shorter than 100 μm cannot be explained by the thermal emission from the large grains, and shows the intensity is significantly larger. Okumura et al. (1999) found that the infrared SED varies with the strength of interstellar radiation field, and the 12–60 μm SED is strongly correlated with that at $\lambda \geq 100 \mu\text{m}$. Shibai et al. (1999) obtained the same result from the Galactic plane data ($|b| < 5$ degree) of COBE/DIRBE. These results suggest that the temperature of the large grain is a key parameter to characterize the Galactic diffuse infrared emission.

Extending the Galactic plane result to external galaxies, one would like to use the largest available database i.e., the IRAS survey (e.g., Soifer et al. 1987). But because of the lack of photometric band at $\lambda > 100 \mu\text{m}$, the IRAS observations alone are not adequate to characterize the emission from dust cooler than 30 K. The ISO and the Submillimeter Common-User Bolometer Array (SCUBA) data have shown that the far-infrared emission from late-type galaxies has a substantial contribution from large grains whose temperature is about 15–25 K (Alton et al. 1998; Haas et al. 1998; Dunne and Eales 2001). If sub-millimeter fluxes are included, the total far-infrared emission increases by a factor of 2–3 with respect to previous estimates based on IRAS data alone (e.g., Helou et al. 1988). The derived large grain temperatures of galaxies are significantly lower than the previous results estimated from the IRAS 60 μm and 100 μm flux densities (e.g., Devereux and Young 1990). Additionally, Devereux and Young (1990) and Alton et al. (1998) also suggested that the dust masses of spiral galaxies derived from sub-millimeter/ISO fluxes are ten times larger than those derived only from the IRAS data. Therefore, the SED at $\lambda > 100 \mu\text{m}$ is crucial to estimate the thermal emission from large grains correctly, and to understand the physical environments in galaxies.

To derive the total infrared luminosities of IRAS galaxies, Xu and Buat (1995) have proposed an empirical relation between the ratio of the integrated far-infrared flux (40 – 120 μm) to the total luminosities (8–1000 μm) and the 60-to-100 μm flux densities ratio from 13 late type galaxies. Here, we chose another approach based on the dust emission properties to derive the total infrared luminosities of IRAS galaxies. We derived the large grain temperatures and the total radiation energies from external galaxies in the far-infrared region by using the relationship between the COBE/DIRBE 60 μm , 100 μm and 140 μm intensities in the Galactic plane derived by Shibai et al. (1999). We also adopted a new empirical model. The present method improves not only the previous evaluation of the far-infrared total luminosities of IRAS galaxies, but also provides the key parameters to characterize galaxies, e.g., the temperature and the dust mass of galaxies.

In this paper, we describe our empirical method to derive the total infrared luminosities of galaxies. The dataset and analysis are explained in Section 2. The results and discussion are presented in Section 3 and Section 4, respectively. We summarize the results and present conclusions in Section 5.

2. Sample and data analysis

2.1. COBE/DIRBE data

We used the COBE/DIRBE ZSMA (Zodi-Subtracted Mission Average) Maps at 60 μm , 100 μm , and 140 μm for the diffuse Galactic emission. These data are available at the Astrophysics Data Facility in the NASA Goddard Space Flight Center (<http://space.gsfc.nasa.gov/astro/cobe>). The reason why we used the three intensities is that

Shibai et al. (1999) and Okumura et al. (1999) have found a correlation between the intensities at 60 μm and that at $\lambda \geq 100 \mu\text{m}$ (100, 140 and 155 μm bands). We selected the area of the Galactic plane at $|b| < 5^\circ$, but the regions where the 60 μm intensities, $I_\nu(60 \mu\text{m}) < 3 \text{ MJy sr}^{-1}$ were omitted in this study to avoid the residual contamination after the subtraction of the Zodiacal light. A total of the omitted areas is 8.5 % of all the selected area. The analysis method used here is the same as that of Shibai et al. (1999). We assumed that the SED at $\lambda \geq 100 \mu\text{m}$ is fitted by a single temperature Planck function with an emissivity index of 2 and applied color-corrections to the intensities at 100 μm and 140 μm . These correction factors are listed in COBE/DIRBE Explanatory supplement version 2.3 (e.g., Appendix B). Then, the corrected intensity $I_\nu^c(\lambda)$ is described simply as

$$I_\nu^c(\lambda) = I_\nu(\lambda)/K_\nu(T_{\text{LG}}) = \tau_{100} \cdot \left(\frac{\nu}{3 \text{ THz}}\right)^2 \cdot B_\nu(T_{\text{LG}}) \quad [\text{W m}^{-2} \text{ Hz}^{-1} \text{ sr}^{-1}], \quad (1)$$

where $K_\nu(T_{\text{LG}})$, τ_{100} , T_{LG} , and $B_\nu(T_{\text{LG}})$ are the color-correction factor for DIRBE dataset, the optical depth at 100 μm , the dust temperature derived from the intensities at 100 μm and 140 μm (“LG” denotes the large grain that is in equilibrium with the ISRF), and the Planck function at temperature T_{LG} , respectively. The dust temperature and the optical thickness are uniquely determined, given the 100 μm and 140 μm intensities. For the temperature range of interest, the color-corrections were less than 8 %.

2.2. Nearby Galaxies

We selected 97 nearby galaxies observed by ISOPHOT and by the Kuiper Airborne Observatory (KAO) from Telesco and Harper (1980), Klaas et al. (1997), Alton et al. (1998), Haas et al. (1998), Siebenmorgen et al. (1999), Calzetti et al. (2000), Contursi et al. (2001), Pérez García and Rodríguez Espinosa (2001), and Tuffs et al. (2002), while the IRAS 60 μm and 100 μm data were taken from IRAS Faint Source Catalog (Version 2), Cataloged Galaxies and Quasars Observed in the IRAS Survey (Version 2), Edelson et al. (1987), Soifer et al. (1989), Xu and Helou (1996), Alton et al. (1998) and Contursi et al. (2001). These published galaxy samples by IRAS, ISOPHOT, and KAO are summarized in Table 1. The sample galaxies collected by us are most of the published data observed at $\lambda > 100 \mu\text{m}$. The present sample contains various types of galaxies, Seyfert galaxies, starbursts, and normal galaxies, etc. The morphological types of the sample galaxies are as follows: 77 spirals, 11 irregulars, and 9 galaxies with other/unknown type. Alton et al. (1998) suggested the possibility that their original ISOPHOT data have a calibration error of +30 %. They gave two reasons for their suggestion: 1) The integrated flux at 200 μm derived from the observation of Engargiola (1991) is smaller than the ISO flux for NGC 6946. 2) They compared the observed 200 μm background with that extrapolated from 100 μm , using the Galactic spectrum at high latitude from Reach et al. (1995), and then obtained the same result as 1). In this paper, we have applied this correction to their data. We used the 150 μm data for three galaxies (NGC 3516, UGC 12138, Mrk 533)

of Pérez García and Rodríguez Espinosa (2001) and the 170 μm data for two galaxies (Mrk 57, CGCG 160139) of Contursi et al. (2001) because the 200 μm flux densities are significantly lower than the 90–150 μm flux densities in the former case (See Figure 2 of Pérez García and Rodríguez Espinosa 2001) and than the 120 and 150 μm flux densities in the latter case (See Figure 6 of Contursi et al. 2001). The data listed in Table 1 are catalog values and need to be applied a color-correction. The correction factors are given in the ISO handbook Volume V (e.g., Appendix C) (Laureijs et al. 2001) and the Infrared Astronomical Satellite Explanatory Supplement (e.g., Section VI) (Beichman et al. 1988). Since the color-correction factor was not available for the KAO 140 μm flux density of M 82, it was not applied. For the SED at $\lambda \geq 100 \mu\text{m}$, we assumed that the dust emissivity index of each sample galaxy is proportional to λ^{-2} , and fitted the two photometric data beyond 100 μm with the following equation:

$$F_{\nu}^c(\lambda) = F_{\nu}(\lambda)/K_{\nu}(T_{\text{LG}}) = \Omega \cdot \tau_{100} \cdot \left(\frac{\nu}{3 \text{ THz}} \right)^2 \cdot B_{\nu}(T_{\text{LG}}) \quad [\text{W m}^{-2} \text{ Hz}^{-1}], \quad (2)$$

where $F_{\nu}(\lambda)$, $F_{\nu}^c(\lambda)$, Ω , and $K_{\nu}(T_{\text{LG}})$ are the catalog flux density in Table 1, the color corrected flux density, the solid angle of the object, and the color-correction factor of IRAS or ISOPHOT, respectively. The other parameters are the same as that in Equation (1). Here we note that Ω and τ_{100} cannot be determined independently. For the temperature range of interest, the corrections to the catalog flux densities were found to be less than 14 %. Haas et al. (1998) and Contursi et al. (2001) have derived temperatures of galaxies from the data at $\lambda \geq 100 \mu\text{m}$ under the same assumption. We confirmed that the values for T_{LG} derived by us are consistent with the temperatures derived by them.

It is noted that we derived the dust temperature, T_{LG} , from color corrected intensities/flux densities by using Equation (1) or (2), whereas use catalogued intensities/flux densities without the color-correction for the other parameters given in subsequent sections i.e., the dust temperature, T_{LG2} , and the intensities/fluxes ratio of Figure 2 and 3.

3. Results

3.1. The Galactic plane

Figure 1 shows the relation between the intensity $\nu I_{\nu}(60 \mu\text{m})$ and the dust temperature, T_{LG} derived from the intensities $I_{\nu}(100 \mu\text{m})$ and $I_{\nu}(140 \mu\text{m})$. Intensity $\nu I_{\nu}(60 \mu\text{m})$ is normalized by the optical depth at 100 μm . The intensity $\nu I_{\nu}(60 \mu\text{m})$ shows a clear power-law dependence. This correlation cannot be fitted by a single temperature Planck function with an emissivity index of 2. We call the simple model of $\lambda^{-2} B_{\nu}(T_{\text{LG}})$ “Model 1.” Okumura et al. (1999) and Shibai et al. (1999) found the following correlation for the Galactic plane far-infrared emission at 60, 100, and 140 or 155 μm .

$$\frac{\nu I_{\nu}(60 \mu\text{m})}{I_{\text{FIR}}} \propto G, \quad (3)$$

where G is the strength of the ISRF given by Equation (4), and I_{FIR} is the total far-infrared

intensity given by Equation (5). They adopted Draine and Lee model (Draine and Lee 1984) which assumes the ratio of average dust absorption efficiency in the ultraviolet to the infrared is 700 in thermal equilibrium. Then, the ISRF strength, G can be written as follows:

$$G = 1.84 \times 10^{-7} \cdot G_0 \cdot T_{\text{LG}}^6 = 2.99 \times 10^{-13} \cdot T_{\text{LG}}^6 \quad [\text{W m}^{-2}], \quad (4)$$

and

$$G_0 = 1.6 \times 10^{-6} \quad [\text{W m}^{-2}],$$

where G_0 is the strength of ISRF in the solar neighborhood (Habing 1968). By Using Equation (4), I_{FIR} is proportional to G as shown by the following relation,

$$I_{\text{FIR}} = \int_0^\infty \tau_{100} \cdot \left(\frac{\nu}{3 \text{ THz}} \right)^2 \cdot B_\nu(T_{\text{LG}}) d\nu \propto \tau_{100} \cdot G \quad [\text{W m}^{-2} \text{ sr}^{-1}]. \quad (5)$$

From Equations (3), (4) and (5), the following relation is derived:

$$\frac{\nu I_\nu(60 \mu\text{m})}{\tau_{100}} = 1.8 \times 10^{-19} \times (T_{\text{LG}})^{12} \quad [\text{W m}^{-2} \text{ sr}^{-1}]. \quad (6)$$

The coefficient of Equation (6) is slightly modified from the original relation derived by Shibai et al. (1999), so as to get a better fit to the data of Figure 1. The relation given by Equation (6) is called “Model 2.”

Figure 2 shows the relation between the dust temperature, T_{LG} , and the ratio, $I_\nu(60 \mu\text{m})/I_\nu(100 \mu\text{m})$. The data points near the brighter end ($I_\nu(60 \mu\text{m})/I_\nu(100 \mu\text{m}) > 0.6$) show the intensities lower than those described by Equation (6) as can be also seen in Figure 1. Here, we present a better fit to the correlation between the ratio, $I_\nu(60 \mu\text{m})/I_\nu(100 \mu\text{m})$, and the dust temperature, T_{LG} , plotted in Figure 2 by employing a simple empirical relation as follows:

$$\frac{I_\nu(60 \mu\text{m})}{I_\nu(100 \mu\text{m})} = \frac{(T_{\text{LG}} - 13.8)}{11.8}. \quad (7)$$

The empirical relation of Equation (7) is called “Model 3.” It is clearly seen that the new relation can fit the data in Figure 2 better than the previous models at $T_{\text{LG}} > 17 \text{ K}$. Although this empirical fit by Model 3 for $T_{\text{LG}} < 17 \text{ K}$ is worse than that for Model 2, it is a minor flaw for the main conclusion because almost all T_{LG} s of external galaxies in our sample are higher than 17 K (See the next section).

Equation (7) suggests that the dust temperature can also be derived from $I_\nu(60 \mu\text{m})$ and $I_\nu(100 \mu\text{m})$ in the Galactic plane. The temperature derived from the 60 and 100 μm bands is called “ T_{LG2} ” to distinguish it from T_{LG} . The derived temperature, T_{LG2} , is given by the following relation:

$$T_{\text{LG2}} = 11.8 \times \frac{I_\nu(60 \mu\text{m})}{I_\nu(100 \mu\text{m})} + 13.8 \quad [\text{K}]. \quad (8)$$

The uncertainty in the estimation of T_{LG2} by Equation (8) is approximately 10 % for $T_{\text{LG}} > 16 \text{ K}$.

3.2. Nearby Galaxies

The dust temperatures derived for the sample galaxies are listed in Table 2. The temperatures of the sample galaxies range from 16 K to 41 K with an average of 24 K. For comparison of T_{LG} and the 60 μm to 100 μm color of nearby galaxies with those of the Galaxy, the mean Galactic plane intensities at 60, 100 and 140 μm were used to derive the color and the temperature, T_{LG} , of the Galactic plane. The derived temperature of the Galaxy is $T_{\text{LG}} \sim 17$ K, and the intensity ratio is $I_\nu(60 \mu\text{m})/I_\nu(100 \mu\text{m}) \sim 0.3$. A majority of the sample galaxies are warmer than the Galactic plane. Figure 3 shows the relation between the ratio, $F_\nu(60 \mu\text{m})/F_\nu(100 \mu\text{m})$, and the dust temperature, T_{LG} . The curve of Model 1 in Figure 3 is changed from that in Figure 2 by the difference in the color-correction factors between IRAS and DIRBE. The difference in the curve is less than 14 % for $T_{\text{LG}} > 30$ K, but from 14 to 40 % for $20 \text{ K} < T_{\text{LG}} < 30 \text{ K}$. The reason why the difference is relatively large for $T_{\text{LG}} < 30 \text{ K}$ is that the difference in the color-correction factors at 60 μm becomes sensitive to that in the detailed spectral shapes between IRAS and DIRBE when the thermal emission in 60 μm band is in the Wien region. For Model 2 and Model 3, the differences in the two curves are small for $16 \text{ K} < T_{\text{LG}} < 50 \text{ K}$ i.e., less than 8.5 %. Therefore, the same curves as in Figure 2 are given in Figure 3. There is a trend that $F_\nu(60 \mu\text{m})/F_\nu(100 \mu\text{m})$ increases with the dust temperature. Most of the data points of galaxies are located between the curves of Model 1 and Model 3 in Figure 3. This trend of the sample galaxies is similar to that of the Galactic plane given by Equation (7). When $T_{\text{LG}} > 25 \text{ K}$, the data points approach the curve of Model 1. The data point of the spiral galaxy, Mrk 993, is significantly apart from the curve given by Equation (7). The flux of Mrk 993 may have a large calibration error since the flux density of IRAS 100 μm of Mrk 993 is more than twice the ISOPHOT 90–200 μm flux densities. Mrk 993 is excluded in the following analysis. This exclusion does not at all affect the main conclusion of this paper.

Next, we derived the dust temperature, T_{LG2} , from $F_\nu(60 \mu\text{m})/F_\nu(100 \mu\text{m})$ by using Equation (8). The derived dust temperature, T_{LG2} , is listed in Table 2. As seen in Figure 3, for a majority of galaxies, the derived temperatures by Equation (2) are larger than T_{LG2} and less than the temperature derived by Model 1. The difference between T_{LG} and T_{LG2} is 1–43 %. The root mean square of the difference ($T_{\text{LG2}} - T_{\text{LG}}$) is 19 %. As the temperatures become higher, the differences become larger. For $T_{\text{LG}} < 25 \text{ K}$, the root mean square of the difference is 14 %, while for $T_{\text{LG}} > 25 \text{ K}$, it is 26 %.

4. Discussion

4.1. Relation between the ratio $F_\nu(60 \mu\text{m})/F_\nu(100 \mu\text{m})$ and T_{LG}

As shown in Figure 3, the relation between the ratio $F_\nu(60 \mu\text{m})/F_\nu(100 \mu\text{m})$ and T_{LG} determined from the spectrum at $\lambda \geq 100 \mu\text{m}$ for the present nearby galaxy sample is similar to that of the Galactic plane. At $\lambda \geq 100 \mu\text{m}$, the diffuse infrared emission from the Galactic plane

is considered to be dominated by thermal emission from large grains, which are in equilibrium with the ISRF (e.g., Mathis 1990). Therefore, the temperature of the large grains depends on the strength of the ambient radiation field. In other words, the far-infrared color at longer wavelengths is the best indicator of the strength of the ISRF in the observed line of sight.

On the other hand, the diffuse infrared emission at $\lambda < 100 \mu\text{m}$ cannot be explained by the thermal emission from large grains. Désert et al. (1990) showed that the $60 \mu\text{m}$ emission comes mainly from very small grains (VSGs). Thus, the $60 \mu\text{m}$ emission and the emission at $\lambda \geq 100 \mu\text{m}$ come from different dust components. Figure 1 indicates that the $60 \mu\text{m}$ intensity normalized by the optical depth at $100 \mu\text{m}$ has a tight correlation with the dust temperature determined by the spectrum at $\lambda \geq 100 \mu\text{m}$, though it consists of intensities in various directions of the Galactic plane. This correlation is well fitted by Equation (7). Since Equation (7) does not have a clear physical basis, we call this a new empirical SED model for the $60 \mu\text{m}$ emission. This implies that the mixing ratio of VSGs with large grains is nearly constant throughout the Galactic plane. Otherwise, we would see much larger scatter in Figures 1 and 2. Sodroski et al. (1997) and Shibai et al. (1999) showed that the far-infrared emission from the Galactic plane is dominated by emission from large grains at $T_{\text{LG}} \sim 17 \text{ K}$ in equilibrium with the ambient ISRF and not by warm dust grains existing in or near discrete H II regions. Therefore, most of the far-infrared radiation of the Galactic plane does not come from discrete H II regions, but from interstellar dust grains diffusely distributed with a uniform temperature heated by the general ISRF. This interpretation is supported by the result that a large fraction of the UV photons from early-type stars in the Galactic plane are not absorbed and form a general ISRF as suggested by Mezger and Smith (1975).

We now apply the new empirical SED model to nearby galaxies. As seen in Figures 2 and 3, these extragalactic objects show the same relation as the Galactic plane. This directly indicates that, for a majority of the galaxies sampled here, the far-infrared emission comes predominantly from the diffuse component heated by the general ISRF like the Galactic plane, and that the far-infrared SED of the galaxies have the same properties as that of the Galactic plane. Thus, the $F_\nu(60 \mu\text{m})/F_\nu(100 \mu\text{m})$ ratio can well be reproduced from the SED at $\lambda \geq 100 \mu\text{m}$, and the infrared SEDs (longer than $100 \mu\text{m}$) can also be reproduced from $F_\nu(60 \mu\text{m})/F_\nu(100 \mu\text{m})$.

Dale et al. (2001) suggested that the infrared SED in the $6\text{--}25 \mu\text{m}$ region of normal galaxies can be reconstructed from the ratio of $F_\nu(60 \mu\text{m})/F_\nu(100 \mu\text{m})$ by an analysis of $6\text{--}100 \mu\text{m}$ SED of 69 normal galaxies. Taking their result, the whole infrared SED longer than $6 \mu\text{m}$ can be described only by the $F_\nu(60 \mu\text{m})/F_\nu(100 \mu\text{m})$ ratio. Recently, Dale and Helou (2002) developed a new SED model of galaxies in the wavelength range from $3 \mu\text{m}$ to 20 cm . This model is based on an empirical characteristic of spectra of galaxies by assuming a simple relation of the dust emissivity to the strength of the interstellar radiation field without physical explanation. In contrast, the present work is unique because it is derived based on observations of the infrared SED of the Galactic plane.

The uniformity in the infrared SED of galaxies suggests that the dust properties are common in galaxies as well as the effective dust-formation processes. Moreover, as described in Section 3, no systematic difference in the infrared SED is seen in different activity/morphological types of galaxies. Pérez García et al. (1998) concluded from their ISOPHOT observations of CfA Seyfert sample that not only the far-infrared SED of starburst galaxies but also the SED of the Seyfert galaxies can be interpreted in terms of the thermal emission from star-forming regions. Negishi et al. (2001) concluded by spectroscopic observations of nearby galaxies with ISO/LWS that there is no difference in far-infrared line ratios between starbursts and AGNs. Accordingly, we propose that the far-infrared SEDs are commonly described by the present empirical model regardless of galaxy type and morphology.

As seen in Figure 3, several galaxies with $T_{\text{LG}} > 25$ K can be fitted better by a single temperature Planck function with the emissivity index of 2 (Model 1) than by Model 3 of Equation (7). This fact indicates that the $60\text{ }\mu\text{m}$ emission is close to the thermal emission from warm large grains in intense interstellar radiation field. It may be the case, if we consider that the contribution of discrete H II regions whose emission peaks at wavelength shorter than $100\text{ }\mu\text{m}$ to the total infrared SED becomes larger in galaxies of higher T_{LG} . For example, the luminous nearby infrared galaxy, M 82, can be well fitted by a single temperature Planck function with the emissivity index of 2 and M 82 lies near the curve of Model 1 as shown in Figure 3. On the other hand, Tol 1924–416 is located close to the present empirical SED model (Equation (7)), while the dust temperature, T_{LG} , is high, 31.4 K. This galaxy is a famous blue compact irregular galaxy, and the star-forming regions of the galaxy do not seem to contain much dust. This is inferred from its low Balmer decrement value $\text{H}\alpha/\text{H}\beta \sim 3.1$ (Storchi-Bergmann et al. 1995). The small dust content of this galaxy allows most of the UV/optical photons radiated by the stars formed to escape from their star-forming clouds easily. These escaped photons contribute to the general interstellar radiation field, and are absorbed by grains in the diffuse interstellar space.

We adopted the value of 2 as the dust emissivity index throughout this paper. This value was derived from the SED of the Galactic Plane (Okumura et al. 1999; Reach et al. 1995), and is naturally predicted by the standard dust grain model (Draine and Lee 1984). Some galaxies reveal smaller values of this index in the far-infrared region, e.g., M 82 (Colbert et al. 1999), Arp 220, Arp 244 and NGC 6240 (Klaas et al. 1997). However, the value of this index does not affect the content of the present paper, if it is between 1 and 2.

4.2. Application to total infrared luminosity

Helou et al. (1988) proposed that the total far-infrared flux in the wavelength region between $40\text{ }\mu\text{m}$ and $120\text{ }\mu\text{m}$, FIR, is given by

$$\text{FIR} = 1.26 \times 10^{-14} \times (2.58 \times F_{\nu}(60\text{ }\mu\text{m}) + F_{\nu}(100\text{ }\mu\text{m})) \quad [\text{W m}^{-2}]. \quad (9)$$

However, as they noted, Equation (9) is valid only when the far-infrared emission that peaks

between 50 and 100 μm . Thus, FIR is limited to an indicator of total far-infrared emission because it neglects the emission at shorter and longer wavelengths. To obtain the total far-infrared integrated flux for $\lambda \geq 40\mu\text{m}$, we define FIR1, derived from the three photometric bands; the 60 μm band and two photometric bands longer than 100 μm . FIR1 is given as follows,

$$\begin{aligned} \text{FIR1} \approx & \int_0^\infty \Omega \cdot \tau_{100} \cdot \left(\frac{\nu}{3 \text{ THz}} \right)^2 \cdot B_\nu(T_{\text{LG}}) d\nu \\ & + \left(F_\nu(60 \mu\text{m}) - B_\nu(\lambda = 60 \mu\text{m}, T_{\text{LG}}) \cdot \Omega \cdot \tau_{100} \cdot \left(\frac{60}{100} \right)^{-2} \right) \cdot \Delta\nu_{60}, \end{aligned} \quad (10)$$

where $B_\nu(\lambda = 60 \mu\text{m}, T_{\text{LG}})$ is the Planck function of the temperature, T_{LG} , at 60 μm , and $\Delta\nu_{60}$ is the frequency width of the IRAS 60 μm band, which corresponds to 3.75×10^{12} Hz. The first term shows the total far-infrared emission from large grains, and the second term shows the contribution of the excess emission in the 60 μm band. Therefore, FIR1 provides a total infrared integrated flux for $\lambda \geq 40 \mu\text{m}$. Here, if the integration of the first term is carried out and $\Omega \cdot \tau_{100}$ is replaced with $F_\nu^c(100 \mu\text{m})/B_\nu(\lambda = 60 \mu\text{m}, T_{\text{LG}})$, then FIR1 can be rewritten by the following relation of $F_\nu(60 \mu\text{m})$, $F_\nu^c(100 \mu\text{m})$ and T_{LG} .

$$\begin{aligned} \text{FIR1} \approx & C_1 \cdot F_\nu(60 \mu\text{m}) + F_\nu^c(100 \mu\text{m}) \times \left(\exp\left(\frac{143.88}{T_{\text{LG}}}\right) - 1 \right) \\ & \times \left(C_2 \cdot T_{\text{LG}}^6 - \frac{C_3}{\exp\left(\frac{239.79}{T_{\text{LG}}}\right) - 1} \right) \quad [10^{-26} \text{ W m}^{-2}], \end{aligned} \quad (11)$$

where C_1 , C_2 , and C_3 are 3.75×10^{12} Hz, $41.2 \text{ Hz} \cdot \text{K}^{-6}$, and 4.82×10^{13} Hz respectively. Both the flux densities of $F_\nu(60 \mu\text{m})$ and $F_\nu^c(100 \mu\text{m})$ are in units of Jansky. Figure 4 shows the comparison of FIR1 with the previous estimate, FIR. The ratio of FIR to FIR1 sharply decreases with T_{LG} at $T_{\text{LG}} < 20$ K. As suggested by Helou et al. (1988), FIR underestimates the total far-infrared flux of galaxy at low temperatures (especially, for $T_{\text{LG}} < 20$ K), although FIR is a good estimator at high temperatures (especially, for $T_{\text{LG}} > 30$ K).

As shown in Section 3, when only the fluxes at 60 and 100 μm are available, the dust temperature, T_{LG2} , of galaxies can be derived from the flux densities at 60 and 100 μm by using Equation (8). Thus, the far-infrared integrated flux can be estimated from Equation (11), when we use T_{LG2} and $F_\nu(100 \mu\text{m})$ instead of T_{LG} and $F_\nu^c(100 \mu\text{m})$. We denote this estimate as FIR2. Figure 5 shows the relation between the ratio of FIR2 to FIR1 and T_{LG} . Figure 5 suggests that FIR2 approximates FIR1 well when $T_{\text{LG}} < 20$ K, and that FIR2 estimates FIR1 with the error between about 0 % and +70 % when $T_{\text{LG}} > 20$ K. The estimated total fluxes, FIR1 and FIR2, are listed in Table 2. For about 70 % of the sample galaxies, the differences between FIR1 and FIR2 are less than 25 % and less than 30 % for 80 % of the sample galaxies. The root mean square of the difference for the entire sample is 26 %. Thus, the total far-infrared integrated flux can be estimated from the IRAS Point Source Catalog and Faint Source Catalog by FIR2 with an uncertainty of 20–30 %. We conclude the present method (FIR2) is more useful than

the previous one (FIR) for $15 \text{ K} < T_{\text{LG}} < 50 \text{ K}$.

The total infrared emission is one of the most crucial indicators of star-forming activity (Sanders and Mirabel 1996; Soifer et al. 1987). Therefore, the present method gives more reliable values for the star formation rate of IRAS galaxies that have only the 60 and 100 μm flux densities. Moreover, other important properties of galaxies, namely, dust mass, averaged general interstellar radiation field, and dust temperature can be estimated solely from the 60 and 100 μm flux densities by using the present method.

5. Conclusion

We have successfully improved the empirical SED model proposed by Okumura et al. (1999) and Shibai et al. (1999) in order to obtain a better fit to the diffuse infrared emission from the Galactic plane. This new model is more accurate at higher color temperature. We applied the model to the infrared SEDs of nearby galaxies observed by IRAS and ISO.

1. We found that the majority of the sample galaxies showed a trend similar to the Galactic plane, but some galaxies approach a single temperature Planck function with the emissivity index of 2 when the large grain temperature, T_{LG} , is higher than 25 K. This fact suggests that for galaxies of $T_{\text{LG}} < 25 \text{ K}$ the diffusely distributed dust grains at a single temperature heated by the general interstellar radiation field dominate as in the Galactic plane, while, for some galaxies of $T_{\text{LG}} > 25 \text{ K}$, discrete warm components from H II regions significantly contribute to the averaged SED in the far-infrared region and possibly dominate the 60 μm and 100 μm bands over the diffuse component.
2. The SED at $\lambda > 100 \mu\text{m}$ can be derived from the flux densities at 60 and 100 μm by the present model. For 96 IRAS galaxies, the uncertainty in the total far-infrared flux for $\lambda \geq 40 \mu\text{m}$ derived from the present method is 26 %. This method allows us to obtain more accurately the important properties of galaxies, such as dust mass, large grain temperature, and total infrared flux of IRAS galaxies.

We thank to Drs. K. Okumura and T. Hirao for their important suggestions, and to the IRTS and ASTRO-F members for useful discussion. We wish to express our gratitude to Dr. T. N. Rengarajan for his critical reading of this paper. We thank Dr. Simone Bianchi, the referee, for his careful reading and useful comments that improved this paper very much. This research has made use of the NASA/IPAC Extragalactic Database (NED), which is operated by the Jet Propulsion Laboratory, California Institute of Technology, under contract with the National Aeronautics and Space Administration. One of the authors (Tsutomu T. Takeuchi) is financially supported by the JSPS Fellowship. This research has been supported in part by a Grant-in-Aid for the Scientific Research Fund (10147102) of the Ministry of Education, Science, Sports and Culture in Japan.

References

- Alton, P. B., Trewhella, M., Davies, J. I., Evans, R., Bianchi, S., Gear, W., Thronson, H., Valentijn, E., & Witt, A. 1998, *A&A*, 335, 807
- Beichman, C. A. 1987, *ARA&A*, 24, 521
- Beichman, C. A., Neugebauer, G., Habing, H. J., Clegg, P. E., & Chester, T. J. 1997, *Infrared Astronomical Satellite Explanatory Supplement* available at NASA Goddard Space Flight Center. (<http://space.gsfc.nasa.gov/astro/iras>)
- Calzetti, D., Armus, L., Bohlin, R. C., Kinney, A. L., Koornneef, J., & Storchi-Bergmann, T. 2000, *ApJ*, 533, 682
- Colbert, J. W., Malkan, M. A., Clegg, P. E., Cox, P., Fischer, J., Lord, S. D., Luhman, M., Satyapal, S., et al. 1999, *ApJ*, 511, 721
- COBE DIRBE Explanatory Supplement. Ver. 2.3, available at NASA Goddard Space Flight Center. (<http://space.gsfc.nasa.gov/astro/cobe>) Colbert, J. W., Malkan, M. A., Clegg, P. E., Cox, P., Fischer, J., Lord, S. D., Luhman, M., Satyapal, S., et al. 1999, *ApJ*, 511, 721
- Contursi, A., Boselli, A., Gavazzi, G., Bertagna, E., Tuffs, R., & Lequeux, J. 2001, *A&A*, 365, 11
- Cox, P., & Mezger, P. G. 1989, *A&A Rev.*, 1, 49
- Dale, D. A., Helou, G., Contursi, A., Silberman, N., & Kolhatkar, S., 2001, *ApJ*, 549, 215
- Dale, D. A., & Helou, G., 2002, *ApJ*, in press
- Désert, F. -X., Boulanger, F., & Puget, J. L. 1990, *A&A*, 237, 215
- Devereux, N. A., & Young, J. S. 1990, *ApJ*, 359, 42
- Draine, B. T., & Lee, H. M. 1984, *ApJ*, 285, 89
- Draine, B. T., & Anderson, N. 1985, *ApJ*, 292, 494
- Dunne, L., & Eales, S. 2001, *MNRAS*, 327, 697
- Dwek, E., Arendt, R. G., Fixsen, D. J., Sodroski, T. J., Odegard, N., Weiland, J. L., Reach, W. T., Hauser, M. G., et al. *ApJ*, 475, 565
- Edelson, R. A., Malkan, M. A., & Rieke, G. H. 1987, *ApJ*, 321, 233
- Engargiola, G. 1991, *ApJS*, 76, 875
- Haas, M., Lemke, D., Stickel, M., Hippelein, H., Kunkel, M., Herbstmeier, U., & Mattila, K. 1998, *A&A*, 338, L33
- Habing, H. J. 1968, *Bull. Astron. Inst. Netherlands*, 19, 421
- Helou, G., Khan, I. R., Malek, L., & Boehmer, L. 1988, *ApJS*, 68, 151
- Klaas, U., Haas, M., Heinrichsen, I., & Schulz, B. 1997, *A&A*, 325, L21
- Laureijs, R. J., Klaas, U., Richards, P. J., Schulz, B., & Ábrahám, P. 2001, *The ISO Handbook*, Vol.5. available at ISO Data Center (<http://www.iso.vilspa.esa.es>)
- Lemke, D., Klaas, U., Abolins, J., Ábrahám, P., Acosta-Pulido, J., Bogun, S., Castaneda, H., Cornwall, L., et al. 1996, *A&A*, 315, L64
- Mathis, J. S. 1990, *ARA&A*, 28, 37
- Mezger, P. G., & Smith, L. F. 1975, in *Proc. of the 3rd European Astronomy Meeting*, Tbilishi, ed. E. K. Kharadze (Georgian: Acad. Sci. Georgian SSR), 369
- Moshir, M., Kopan, G., Conrow, T., McCallon, H., Hacking, P., Gregorich, D., Rohrbach, G., Melnyk, M., Rice, W., Fullmer, L., et al. 1990, *The IRAS Faint Source Catalog*, Version 2

- Negishi, T., Onaka, T., Chan, K. -W., & Roellig, T. L. 2001, *A&A*, 375, 566
- Okumura, K., Hiromoto, N., Shibai, H., Onaka, T., Makiuchi, S., Matsuhara, H., Nakagawa, T., & Okuda, H. 1999, in *Star Formation 1999*, ed. T. Nakamoto (Nobeyama: Nobeyama Radio Observatory), 97
- Pérez García, A. M., Rodríguez Espinosa, J. M., & Santolaya Rey, A. E. 1998, *ApJ*, 500, 685
- Pérez García, A. M., & Rodríguez Espinosa, J. M. 2001, *ApJ*, 557, 39
- Reach, W. T., Dwek, E., Fixsen, D. J., Hewagama, T., Mather, J. C., Shafer, R. A., Banday, A. J., Bennett, C. L., et al. 1995, *ApJ*, 415, 188
- Sanders, D. B., & Mirabel, I. F. 1996, *ARA&A*, 34, 749
- Siebenmorgen, R., Krügel, E., & Chini, R. 1999, *A&A*, 351, 495
- Shibai, H., Okumura, K., & Onaka, T. 1999, in *Star Formation 1999*, ed. T. Nakamoto (Nobeyama: Nobeyama Radio Observatory), 67
- Soifer, B. T., Houck, J. R., & Neugebauer, G. 1987, *ARA&A*, 25, 187
- Soifer, B. T., Boehmer, L., Neugebauer, G., Sanders, D. B. 1989, *AJ*, 98, 766
- Sodroski, T. J., Odegard, N., Arendt, R. G., Dwek, E., Weiland, J. L., Hauser, M. G., & Kelsall, T. 1997, *ApJ*, 480, 173
- Storchi-Bergmann, T., Kinney, A. L., & Challis, P. 1995, *ApJS*, 98, 103
- Telesco, C. M., & Harper, D. A. 1980, *ApJ*, 235, 392
- Tuffs, R. J., Popescu, C. C., Pierini, D., Völk, H. J., Hippelein, H., Leech, K., Metcalfe, L., Heinrichsen, I., & Xu, C. 2002, *ApJS*, 139, 37
- Xu, C., & Buat, V., 1995, *A&A*, 293, L65
- Xu, C., & Helou, G., 1996, *ApJ*, 456, 152

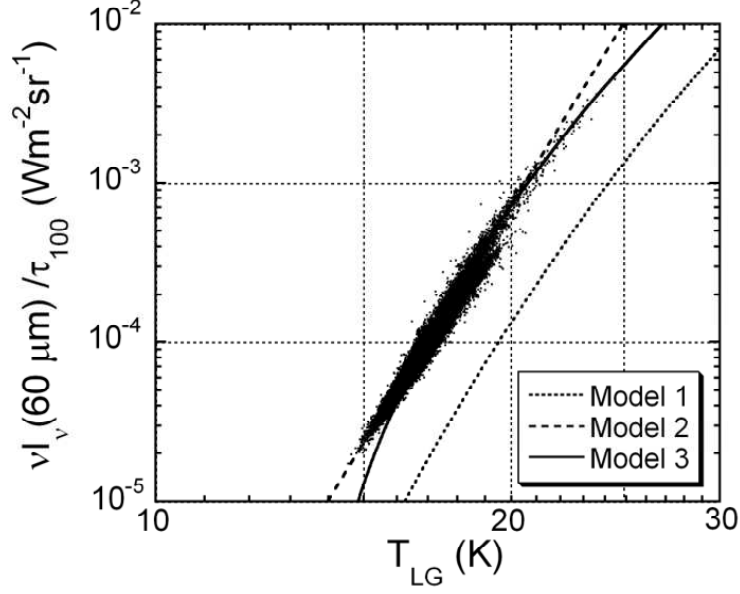


Fig. 1. Plot of the DIRBE 60 μm intensity normalized by the 100 μm optical depth, $\nu I_\nu(60 \mu\text{m})/\tau_{100}$, vs. the dust temperature, T_{LG} , derived from the DIRBE 100 μm and 140 μm intensities for the Galactic plane in the region within 5 degree from the Galactic equator. The three curves in this figure indicate the relations between $\nu I_\nu(60 \mu\text{m})/\tau_{100}$ and T_{LG} derived from the three SED models, respectively. The dotted curve (Model 1) indicates that derived from a single temperature Planck function with an emissivity index of 2. The dashed curve (Model 2) indicates that derived from the relation described as Equation (3). The solid curve (Model 3) indicates that given by the present empirical relation described as Equation (7).

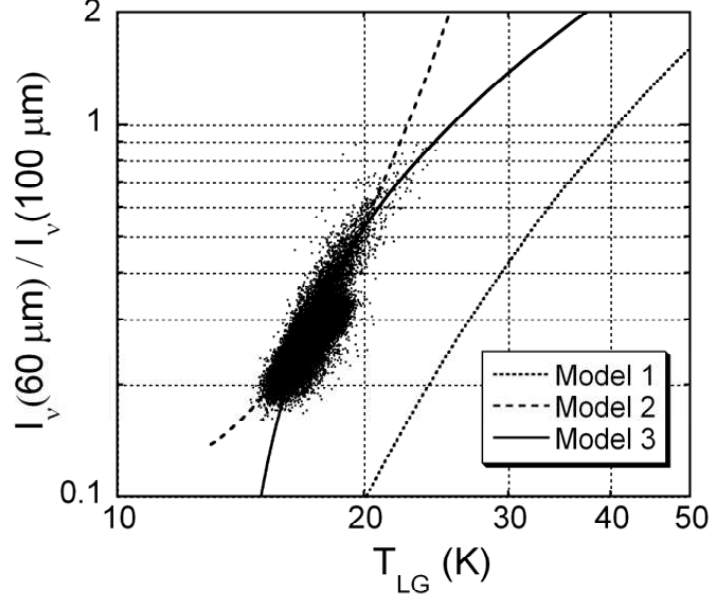


Fig. 2. Plot of the ratio of DIRBE 60 μm to 100 μm intensities, $I_\nu(60 \mu\text{m})/I_\nu(100 \mu\text{m})$, vs. the dust temperature, T_{LG} , derived from the DIRBE 100 μm and 140 μm intensities for the Galactic plane in the region within 5 degree from the Galactic equator. The three curves in this figure indicate the relations between $I_\nu(60 \mu\text{m})/I_\nu(100 \mu\text{m})$ and T_{LG} derived from the same three SED models as in Figure 1.

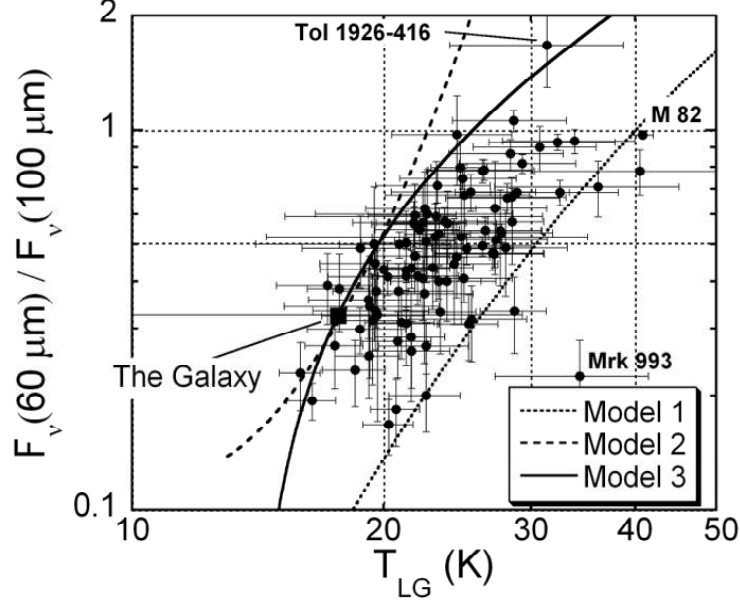


Fig. 3. Plot of the ratio of IRAS 60 μm to 100 μm flux densities, $F_\nu(60 \mu\text{m})/F_\nu(100 \mu\text{m})$, vs. the dust temperature, T_{LG} , derived from the IRAS flux density at 100 μm and the ISOPHOT (KAO) flux density at $\lambda > 100 \mu\text{m}$ for the galaxy sample listed in Table 1. The data points of solid circle are galaxies of Table 1, and the error bars of the sample galaxies are the 1σ uncertainty. The data point of solid square symbol is derived from the three bands (60 μm , 100 μm , 140 μm) dataset which are the mean intensities of the Galactic plane in the region within 5 degrees from the Galactic equator. The three curves in this figure indicate the relations between $F_\nu(60 \mu\text{m})/F_\nu(100 \mu\text{m})$ and T_{LG} derived from the same three SED models as in Figure 1.

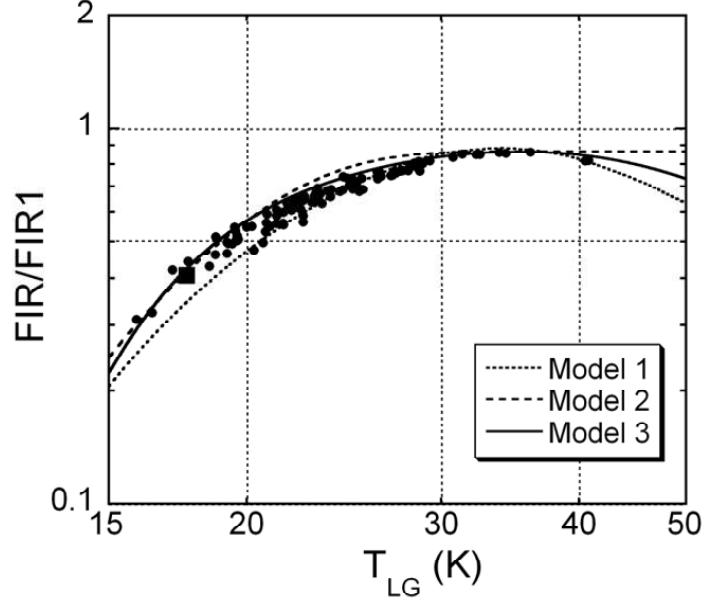


Fig. 4. The ratio of FIR/FIR1 vs. T_{LG} for the galaxy sample listed in Table 1. FIR is the total infrared flux in the wavelength region between 40 and 120 μm given by Helou et al. (1988). FIR1 is the total infrared flux for $\lambda \geq 40 \mu\text{m}$ derived from Equation (11). The dust temperature, T_{LG} , is the same as in Figure 3. The symbols of data points are the same as in Figure 3. The three curves in this figure indicate the relations between FIR/FIR1 and T_{LG} derived from the same three SED models as in Figure 1.

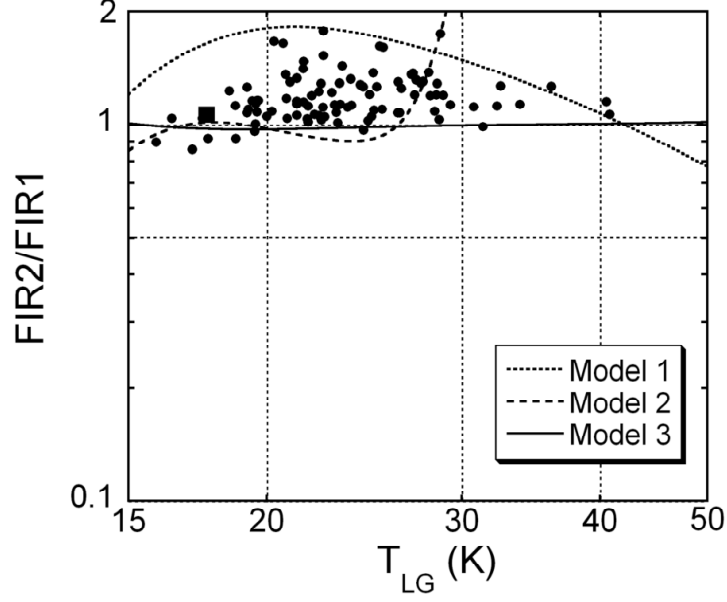


Fig. 5. The ratio of FIR2/FIR1 vs. T_{LG} for the galaxy sample listed in Table 1. FIR1 is the total infrared flux for $\lambda \geq 40 \mu\text{m}$ derived from Equation (11). FIR2 is the estimate of FIR1 derived from the IRAS 60 and $100 \mu\text{m}$ flux densities by using Equation (7). The dust temperature, T_{LG} , is the same as in Figure 3. The symbols of data points are the same as in Figure 3. The three curves in this figure indicate the relations between FIR2/FIR1 and T_{LG} derived from the same three SED models as in Figure 1.

Table 1. Galaxy data

Galaxy name	$^*F_\nu(60\ \mu\text{m})$ (Jy)	$^*F_\nu(100\ \mu\text{m})$ (Jy)	$^\dagger F_\nu(150\ \mu\text{m})$ (Jy)	$^\dagger F_\nu(170\ \mu\text{m})$ (Jy)	$^\dagger F_\nu(200\ \mu\text{m})$ (Jy)	‡ Refs.
NGC 134	22.4 ± 3.4	67.0 ± 10.1	-	-	89 ± 27	(c)
M 31	595 ± 28	3073 ± 316	-	7900 ± 800	-	(d), (n)
Mrk 555	4.22 ± 0.27	8.68 ± 0.52	-	-	5.3 ± 1.6	(e), (j)
IC 1586	0.96 ± 0.08	1.69 ± 0.19	2.11 ± 0.52	-	-	(f), (j)
Mrk 993	0.27 ± 0.05	1.32 ± 0.24	-	-	0.39 ± 0.12	(h), (j)
NGC 628	26.3 ± 3.9	67.5 ± 10.1	-	-	146 ± 44	(c)
NGC 660	71.4 ± 10.7	120 ± 18	-	-	111 ± 33	(c)
UGC 1395	0.47 ± 0.05	1.24 ± 0.17	-	-	1.33 ± 0.40	(h), (l)
NGC 1068	176 ± 9	224 ± 9	-	-	120.8 ± 36.2	(h), (j)
UGC 2936	4.49 ± 0.23	10.96 ± 0.99	-	-	13.0 ± 3.9	(e), (j)
UGC 2982	8.35 ± 0.25	16.89 ± 0.85	-	-	9.2 ± 2.8	(e), (j)
M 82	1313 ± 1	1355 ± 1	$^{\S}630 \pm 24$	-	-	(a), (m)
Mrk 1243	0.35 ± 0.05	0.87 ± 0.15	-	-	0.62 ± 0.17	(h), (j)
NGC 3079	44.50 ± 2.67	89.22 ± 4.46	-	-	95.12 ± 28.54	(h), (j)
NGC 3227	7.83 ± 0.39	17.59 ± 0.88	-	-	23.43 ± 7.03	(h), (j)
UGC 6100	0.63 ± 0.06	1.53 ± 0.20	-	-	1.38 ± 0.41	(h), (l)
NGC 3516	1.76 ± 0.07	2.26 ± 0.29	1.11 ± 0.33	-	-	(h), (j)
CGCG 97079	0.39 ± 0.08	0.65 ± 0.16	-	-	0.54 ± 0.35	(g)
UGC 6697 (CGCG 97087)	1.58 ± 0.24	3.41 ± 0.53	-	-	2.25 ± 0.36	(g)
NGC 3982	6.57 ± 0.53	15.23 ± 1.22	-	-	14.45 ± 4.34	(h), (j)
Arp 244	39.47 ± 2.37	72.30 ± 6.51	-	-	64.1 ± 19.2	(b), (j)
NGC 4051	7.13 ± 0.93	23.92 ± 1.20	-	-	36.90 ± 11.07	(h), (j)
NGC 4151	6.72 ± 0.34	8.60 ± 0.43	-	-	4.69 ± 1.41	(h), (l)
NGC 4178 (VCC 66)	1.54 ± 0.25	8.39 ± 1.01	-	11.27 ± 0.03	-	(i), (k)
NGC 4192 (VCC 92)	5.11 ± 0.82	18.94 ± 3.03	-	40.29 ± 0.50	-	(i), (k)
NGC 4207 (VCC 152)	3.03 ± 0.48	7.46 ± 1.19	-	8.38 ± 0.38	-	(i), (k)
NGC 4235	0.32 ± 0.04	0.65 ± 0.14	-	-	0.30 ± 0.09	(h), (j)
Mrk 766	4.03 ± 0.28	4.66 ± 0.28	-	-	2.10 ± 0.63	(h), (j)
VCC 459	0.24 ± 0.04	0.54 ± 0.14	-	0.50 ± 0.03	-	(i), (j)
NGC 4293 (VCC 460)	4.62 ± 0.74	10.63 ± 1.70	-	11.25 ± 1.10	-	(i), (k)
NGC 4344 (VCC 655)	0.43 ± 0.07	1.88 ± 0.23	-	5.36 ± 0.03	-	(i), (k)
UGC 7470 (VCC 664)	0.49 ± 0.08	0.86 ± 0.17	-	0.97 ± 0.03	-	(i), (k)
NGC 4351 (VCC 692)	0.73 ± 0.12	1.91 ± 0.31	-	3.91 ± 0.09	-	(i), (k)
NGC 4388	10.24 ± 0.82	18.10 ± 1.27	-	-	16.78 ± 5.03	(h), (j)

Table 1. (Continued)

Galaxy name	$^*F_\nu(60\ \mu\text{m})$ (Jy)	$^*F_\nu(100\ \mu\text{m})$ (Jy)	$^\dagger F_\nu(150\ \mu\text{m})$ (Jy)	$^\dagger F_\nu(170\ \mu\text{m})$ (Jy)	$^\dagger F_\nu(200\ \mu\text{m})$ (Jy)	‡ Refs.
NGC 4394 (VCC 857)	1.01 ± 0.12	4.34 ± 0.69	-	7.76 ± 0.18	-	(i), (k)
NGC 4402 (VCC 873)	5.80 ± 0.93	17.47 ± 2.80	-	17.72 ± 0.29	-	(i), (k)
NGC 4413 (VCC 912)	1.02 ± 0.12	3.31 ± 0.53	-	2.82 ± 0.10	-	(i), (k)
NGC 4423 (VCC 971)	0.47 ± 0.08	1.10 ± 0.14	-	1.38 ± 0.09	-	(i), (j)
NGC 4430 (VCC 1002)	1.11 ± 0.13	4.01 ± 0.64	-	5.30 ± 0.11	-	(i), (k)
NGC 4429 (VCC 1003)	1.54 ± 0.25	4.62 ± 0.74	-	3.12 ± 0.06	-	(i), (k)
NGC 4438 (VCC 1043)	4.08 ± 0.49	10.82 ± 1.73	-	16.72 ± 0.59	-	(i), (k)
NGC 4450 (VCC 1110)	1.19 ± 0.14	7.12 ± 0.85	-	10.01 ± 0.17	-	(i), (k)
UGC 7621 (VCC 1189)	0.23 ± 0.06	0.73 ± 0.14	-	1.16 ± 0.03	-	(i), (j)
NGC 4477 (VCC 1253)	0.59 ± 0.07	1.11 ± 0.13	-	1.13 ± 0.09	-	(i), (k)
NGC 4491 (VCC 1326)	2.64 ± 0.32	3.31 ± 0.40	-	2.98 ± 0.31	-	(i), (k)
NGC 4498 (VCC 1379)	1.20 ± 0.14	3.86 ± 0.62	-	4.98 ± 0.15	-	(i), (k)
NGC 4502 (VCC 1410)	0.23 ± 0.06	0.62 ± 0.14	-	0.69 ± 0.04	-	(i), (j)
UGC 7695 (VCC 1450)	1.30 ± 0.16	3.15 ± 0.38	-	3.96 ± 0.13	-	(i), (k)
NGC 4531 (VCC 1552)	0.35 ± 0.05	1.75 ± 0.25	-	1.94 ± 0.13	-	(i), (j)
NGC 4532 (VCC 1554)	8.95 ± 1.43	15.64 ± 2.50	-	10.65 ± 0.19	-	(i), (k)
UGC 7736 (VCC 1575)	1.07 ± 0.13	2.30 ± 0.37	-	2.74 ± 0.14	-	(i), (k)
NGC 4569 (VCC 1690)	7.21 ± 1.15	23.36 ± 3.74	-	29.16 ± 0.32	-	(i), (k)
NGC 4579 (VCC 1727)	4.54 ± 0.73	17.91 ± 2.87	-	29.19 ± 1.20	-	(i), (k)
NGC 4580 (VCC 1730)	1.17 ± 0.14	4.48 ± 0.72	-	5.46 ± 0.55	-	(i), (k)
Mrk 53 (CGCG 160020)	0.65 ± 0.11	1.05 ± 0.20	-	-	0.89 ± 0.31	(g)
Mrk 231	31.99 ± 1.60	30.29 ± 1.21	-	-	13.34 ± 4.00	(h), (j)
IC 3913 (CGCG 160026)	0.26 ± 0.06	0.44 ± 0.14	-	-	0.34 ± 0.27	(g)
NGC 4848 (CGCG 160055)	1.40 ± 0.22	2.75 ± 0.43	-	-	2.31 ± 0.35	(g)
Mrk 57 (CGCG 160067)	0.45 ± 0.08	0.83 ± 0.18	-	0.60 ± 0.05	-	(g)
CGCG 160086	0.15 ± 0.05	0.46 ± 0.14	-	-	0.60 ± 0.60	(g)
UGC 8118 (CGCG 160088)	0.25 ± 0.06	0.88 ± 0.18	-	-	0.84 ± 0.15	(g)
IC 4040 (CGCG 160252)	1.38 ± 0.21	2.64 ± 0.41	-	-	2.06 ± 0.76	(g)
NGC 4911 (CGCG 160260)	0.78 ± 0.13	2.46 ± 0.39	-	-	1.45 ± 0.47	(g)
NGC 4921 (CGCG 160095)	0.23 ± 0.06	0.67 ± 0.16	-	-	0.94 ± 0.37	(g)
CGCG 160128	0.22 ± 0.06	0.44 ± 0.14	-	-	0.59 ± 0.30	(g)
CGCG 160127	0.23 ± 0.06	0.44 ± 0.14	-	-	0.28 ± 0.25	(g)
CGCG 160139	0.36 ± 0.07	0.58 ± 0.15	-	0.43 ± 0.05	-	(g)
NGC 5033	16.45 ± 0.1	50.81 ± 0.1	-	-	66.93 ± 20.08	(h), (m)
Mrk 66	0.54 ± 0.04	0.80 ± 0.15	0.77 ± 0.19	-	-	(f), (j)

Table 1. (Continued)

Galaxy name	$^*F_\nu(60\ \mu\text{m})$ (Jy)	$^*F_\nu(100\ \mu\text{m})$ (Jy)	$^\dagger F_\nu(150\ \mu\text{m})$ (Jy)	$^\dagger F_\nu(170\ \mu\text{m})$ (Jy)	$^\dagger F_\nu(200\ \mu\text{m})$ (Jy)	‡ Refs.
NGC 5194	130 ± 19	303 ± 45	-	-	373 ± 112	(c)
NGC 5236	314 ± 47	624 ± 94	-	-	622 ± 187	(c)
UGC 8621	1.07 ± 0.08	2.63 ± 0.30	-	-	1.64 ± 0.49	(h), (l)
NGC 5252	0.43 ± 0.06	0.75 ± 0.13	-	-	0.53 ± 0.16	(h), (l)
Mrk 266	7.34 ± 0.44	11.07 ± 0.78	-	-	5.11 ± 1.53	(h), (j)
Mrk 461	0.44 ± 0.06	0.46 ± 0.11	-	-	0.30 ± 0.09	(h), (l)
Mrk 279	1.26 ± 0.06	2.20 ± 0.15	-	-	1.59 ± 0.48	(h), (j)
Mrk 799	10.41 ± 0.42	19.47 ± 0.80	-	-	9.3 ± 2.8	(e), (j)
IC 4397	1.54 ± 0.11	3.25 ± 0.23	-	-	1.65 ± 0.50	(h), (j)
NGC 5548	1.07 ± 0.09	1.61 ± 0.16	-	-	0.72 ± 0.22	(h), (j)
Mrk 817	2.12 ± 0.09	2.27 ± 0.14	-	-	0.69 ± 0.21	(h), (j)
NGC 5719	8.06 ± 0.48	17.10 ± 0.86	-	-	8.6 ± 2.6	(e), (j)
NGC 5860	1.64 ± 0.08	3.02 ± 0.18	2.63 ± 0.65	-	-	(f), (j)
Arp 220	103.8 ± 4.2	112.4 ± 3.4	-	-	37.6 ± 11.3	(b), (j)
NGC 6090	6.66 ± 0.26	8.94 ± 0.45	8.67 ± 2.15	-	-	(f), (j)
NGC 6104	0.48 ± 0.05	1.79 ± 0.21	-	-	1.50 ± 0.45	(h), (l)
NGC 6240	22.68 ± 0.91	27.78 ± 1.11	-	-	11.6 ± 3.5	(b), (j)
Tol 1924-416	1.69 ± 0.10	1.01 ± 0.22	0.68 ± 0.17	-	-	(f), (j)
NGC 6918	9.32 ± 0.56	13.62 ± 0.68	-	-	4.5 ± 1.4	(e), (j)
NGC 6946	165 ± 25	338 ± 51	-	-	520 ± 156	(c)
NGC 7331	42.9 ± 6.4	120 ± 18	-	-	170 ± 51	(c)
UGC 12138	0.90 ± 0.08	1.27 ± 0.19	0.71 ± 0.21	-	-	(h), (l)
Mrk 323	3.16 ± 0.22	7.91 ± 0.55	-	-	6.0 ± 1.8	(e), (j)
NGC 7673	4.91 ± 0.34	6.89 ± 0.48	7.60 ± 1.90	-	-	(f), (j)
Mrk 533	5.59 ± 0.50	8.15 ± 0.57	7.61 ± 2.28	-	-	(h), (j)
Mrk 534	7.28 ± 0.04	10.65 ± 0.12	-	-	4.6 ± 1.4	(e), (m)
Mrk 538	10.36 ± 1.24	11.51 ± 0.69	-	-	4.3 ± 1.3	(e), (j)
Mrk 332	4.87 ± 0.34	9.49 ± 0.67	-	-	4.7 ± 1.4	(e), (j)

*Flux densities at 60 and 100 μm from IRAS data (which are not color corrected). The 1 σ uncertainties are also reported.

† Flux densities at 150, 170 and 200 μm from ISOPHOT and KAO data (which are also not color corrected). The 1 σ uncertainties are also reported.

‡ References of the sample of (a) Telesco and Harper (1980); (b) Klaas et al. (1997); (c) Alton et al. (1998); (d) Haas et al. (1998); (e) Siebenmorgen et al. (1999); (f) Calzetti et al. (2000); (g) Contursi et al. (2001); (h) Pérez García and Rodríguez Espinosa (2001); (i) Tuffs et al. (2002); (j) IRAS Faint Source Catalog Version 2; (k) Cataloged Galaxies and Quasars Observed in the IRAS Survey Version 2; (l) Edelson et al. (1987); (m) Soifer et al. (1989); (n) Xu and Helou (1996).

§ The flux density of M 82 in the 150 μm column of this table is not that of 150 μm but of 140 μm .

Table 2. Results

Galaxy name	T_{LG} (K)	T_{LG2} (K)	FIR (W/m^2)	FIR1 (W/m^2)	FIR2 (W/m^2)
NGC 134	19.6 ± 3.1	17.7	1.57E-12	3.13E-12	3.56E-12
M 31	16.4 ± 1.1	16.1	5.81E-11	1.80E-10	1.87E-10
Mrk 555	25.2 ± 3.4	19.5	2.47E-13	3.49E-13	4.41E-13
IC 1586	21.8 ± 3.4	20.5	5.26E-14	8.34E-14	8.61E-14
Mrk 993	34.3 ± 7.2	16.4	2.63E-14	3.07E-14	7.70E-14
NGC 628	17.1 ± 2.3	18.4	1.71E-12	4.07E-12	3.50E-12
NGC 660	21.8 ± 2.6	20.8	3.83E-12	6.03E-12	6.14E-12
UGC 1395	20.8 ± 3.4	18.2	3.08E-14	5.50E-14	6.45E-14
NGC 1068	26.4 ± 3.8	23.1	8.54E-12	1.12E-11	1.20E-11
UGC 2936	20.2 ± 3.1	18.6	2.84E-13	5.19E-13	5.64E-13
UGC 2982	26.3 ± 3.8	19.6	4.84E-13	6.60E-13	8.58E-13
M 82	40.8 ± 1.2	25.2	5.98E-11	7.31E-11	7.77E-11
Mrk 1243	23.8 ± 3.4	18.5	2.24E-14	3.41E-14	4.51E-14
NGC 3079	20.9 ± 3.2	19.7	2.57E-12	4.36E-12	4.53E-12
NGC 3227	19.5 ± 2.8	19.1	4.76E-13	8.95E-13	8.99E-13
UGC 6100	22.0 ± 2.6	18.7	3.98E-14	6.58E-14	7.87E-14
NGC 3516	40.5 ± 10.2	23.0	8.57E-14	1.05E-13	1.21E-13
CGCG 97079	22.6 ± 6.0	20.9	2.09E-14	3.17E-14	3.33E-14
UGC 6697 (CGCG 97087)	24.5 ± 2.3	19.3	9.43E-14	1.38E-13	1.74E-13
NGC 3982	21.6 ± 2.4	18.9	4.05E-13	6.78E-13	7.78E-13
Arp 244	22.1 ± 2.6	20.2	2.20E-12	3.46E-12	3.68E-12
NGC 4051	18.7 ± 2.5	17.3	5.33E-13	1.16E-12	1.30E-12
NGC 4151	26.3 ± 3.8	23.0	3.27E-13	4.29E-13	4.61E-13
NGC 4178 (VCC 66)	20.7 ± 1.4	16.0	1.56E-13	3.15E-13	5.17E-13
NGC 4192 (VCC 92)	17.5 ± 1.4	17.0	4.05E-13	1.01E-12	1.05E-12
NGC 4207 (VCC 152)	22.3 ± 2.3	18.6	1.93E-13	3.14E-13	3.84E-13
NGC 4235	28.0 ± 5.2	19.6	1.84E-14	2.39E-14	3.28E-14
Mrk 766	28.4 ± 4.4	24.0	1.90E-13	2.36E-13	2.57E-13
VCC 459	24.3 ± 3.1	19.0	1.46E-14	2.16E-14	2.76E-14
NGC 4293 (VCC 460)	22.9 ± 2.7	18.9	2.84E-13	4.46E-13	5.44E-13
NGC 4344 (VCC 655)	15.9 ± 0.9	16.5	3.77E-14	1.22E-13	1.09E-13
UGC 7470 (VCC 664)	22.3 ± 2.7	20.5	2.68E-14	4.15E-14	4.38E-14
NGC 4351 (VCC 692)	17.7 ± 1.5	18.3	4.78E-14	1.08E-13	9.92E-14
NGC 4388	21.8 ± 2.4	20.5	5.60E-13	8.89E-13	9.22E-13
NGC 4394 (VCC 857)	18.5 ± 1.6	16.5	8.75E-14	2.04E-13	2.51E-13

Table 2. (Continued)

Galaxy name	T_{LG} (K)	T_{LG2} (K)	FIR (W/m ²)	FIR1 (W/m ²)	FIR2 (W/m ²)
NGC 4402 (VCC 873)	23.4 ± 2.4	17.7	4.09E-13	6.50E-13	9.29E-13
NGC 4413 (VCC 912)	25.3 ± 2.1	17.4	7.49E-14	1.11E-13	1.79E-13
NGC 4423 (VCC 971)	21.3 ± 1.8	18.8	2.91E-14	4.96E-14	5.64E-14
NGC 4430 (VCC 1002)	20.8 ± 2.0	17.1	8.66E-14	1.63E-13	2.22E-13
NGC 4429 (VCC 1003)	28.7 ± 2.6	17.7	1.08E-13	1.41E-13	2.45E-13
NGC 4438 (VCC 1043)	19.6 ± 1.8	18.3	2.69E-13	5.20E-13	5.63E-13
NGC 4450 (VCC 1110)	20.3 ± 1.4	15.8	1.28E-13	2.71E-13	4.50E-13
UGC 7621 (VCC 1189)	19.4 ± 2.1	17.5	1.67E-14	3.39E-14	3.92E-14
NGC 4477 (VCC 1253)	23.3 ± 2.1	20.1	3.32E-14	4.98E-14	5.64E-14
NGC 4491 (VCC 1326)	24.7 ± 1.9	23.2	1.28E-13	1.74E-13	1.78E-13
NGC 4498 (VCC 1379)	21.0 ± 2.0	17.5	8.76E-14	1.60E-13	2.08E-13
NGC 4502 (VCC 1410)	22.4 ± 3.2	18.2	1.53E-14	2.52E-14	3.23E-14
UGC 7695 (VCC 1450)	21.3 ± 1.6	18.7	8.20E-14	1.40E-13	1.62E-13
NGC 4531 (VCC 1552)	22.5 ± 2.2	16.2	3.34E-14	5.94E-14	1.05E-13
NGC 4532 (VCC 1554)	28.5 ± 2.6	20.6	4.88E-13	6.20E-13	7.97E-13
UGC 7736 (VCC 1575)	21.8 ± 2.2	19.3	6.38E-14	1.04E-13	1.17E-13
NGC 4569 (VCC 1690)	21.3 ± 2.0	17.4	5.29E-13	9.50E-13	1.26E-12
NGC 4579 (VCC 1727)	19.2 ± 1.7	16.8	3.73E-13	8.04E-13	1.01E-12
NGC 4580 (VCC 1730)	21.6 ± 2.4	16.9	9.45E-14	1.71E-13	2.51E-13
Mrk 53 (CGCG 160020)	22.4 ± 3.4	21.1	3.44E-14	5.23E-14	5.39E-14
Mrk 231	28.6 ± 4.5	26.3	1.42E-12	1.75E-12	1.80E-12
IC 3913 (CGCG 160026)	23.1 ± 7.9	20.8	1.40E-14	2.09E-14	2.25E-14
NGC 4848 (CGCG 160055)	22.5 ± 1.9	19.8	8.02E-14	1.25E-13	1.40E-13
Mrk 57 (CGCG 160067)	27.6 ± 3.4	20.2	2.51E-14	3.27E-14	4.22E-14
CGCG 160086	19.7 ± 9.6	17.6	1.07E-14	2.12E-14	2.45E-14
UGC 8118 (CGCG 160088)	21.6 ± 2.1	17.2	1.92E-14	3.44E-14	4.84E-14
IC 4040 (CGCG 160252)	23.0 ± 3.7	20.0	7.81E-14	1.19E-13	1.34E-13
NGC 4911 (CGCG 160260)	25.5 ± 4.2	17.5	5.64E-14	8.23E-14	1.32E-13
NGC 4921 (CGCG 160095)	19.3 ± 4.0	17.9	1.59E-14	3.22E-14	3.54E-14
CGCG 160128	19.5 ± 5.4	19.7	1.27E-14	2.33E-14	2.24E-14
CGCG 160127	24.8 ± 10.3	20.0	1.30E-14	1.86E-14	2.24E-14
CGCG 160139	27.2 ± 4.1	21.1	1.90E-14	2.48E-14	2.98E-14
NGC 5033	19.6 ± 2.7	17.6	1.18E-12	2.34E-12	2.71E-12
Mrk 66	25.0 ± 4.9	21.7	2.76E-14	3.80E-14	4.16E-14
NGC 5194	20.0 ± 3.2	18.9	8.04E-12	1.48E-11	1.55E-11
NGC 5236	21.3 ± 2.5	19.7	1.81E-11	2.99E-11	3.17E-11

Table 2. (Continued)

Galaxy name	T_{LG} (K)	T_{LG2} (K)	FIR (W/m ²)	FIR1 (W/m ²)	FIR2 (W/m ²)
UGC 8621	25.0 ± 3.6	18.6	6.79E-14	9.88E-14	1.35E-13
NGC 5252	23.9 ± 3.4	20.5	2.33E-14	3.39E-14	3.82E-14
Mrk 266	28.1 ± 4.4	21.6	3.78E-13	4.81E-13	5.75E-13
Mrk 461	24.5 ± 4.0	25.3	2.01E-14	2.71E-14	2.62E-14
Mrk 279	23.7 ± 3.0	20.6	6.87E-14	1.01E-13	1.12E-13
Mrk 799	27.7 ± 4.2	20.1	5.84E-13	7.59E-13	9.90E-13
IC 4397	27.0 ± 4.0	21.6	5.51E-14	6.94E-14	8.34E-14
NGC 5548	28.5 ± 4.6	19.4	9.10E-14	1.22E-13	1.65E-13
Mrk 817	33.9 ± 6.1	24.8	9.75E-14	1.13E-13	1.28E-13
NGC 5719	27.1 ± 4.0	19.4	4.77E-13	6.37E-13	8.70E-13
NGC 5860	26.5 ± 4.4	20.2	9.14E-14	1.23E-13	1.54E-13
Arp 220	32.3 ± 5.5	24.8	4.79E-12	5.64E-12	6.32E-12
NGC 6090	24.9 ± 4.0	22.6	3.29E-13	4.50E-13	4.73E-13
NGC 6104	22.5 ± 2.8	17.0	3.82E-14	6.54E-14	9.97E-14
NGC 6240	29.3 ± 4.7	23.4	1.09E-12	1.34E-12	1.51E-12
Tol 1924-416	31.4 ± 7.4	33.5	6.77E-14	7.96E-14	7.85E-14
NGC 6918	32.5 ± 5.7	21.9	4.75E-13	5.59E-13	7.09E-13
NGC 6946	18.8 ± 2.8	19.6	9.62E-12	1.87E-11	1.72E-11
NGC 7331	19.2 ± 2.9	18.0	2.91E-12	5.86E-12	6.29E-12
UGC 12138	36.1 ± 9.0	22.2	4.53E-14	5.26E-14	6.65E-14
Mrk 323	23.3 ± 2.9	18.5	2.02E-13	3.16E-13	4.08E-13
NGC 7673	23.2 ± 3.6	22.2	2.47E-13	3.58E-13	3.62E-13
Mrk 533	25.4 ± 5.0	21.9	2.84E-13	3.86E-13	4.24E-13
Mrk 534	28.9 ± 4.5	21.9	3.71E-13	4.63E-13	5.54E-13
Mrk 538	30.8 ± 5.2	24.4	4.82E-13	5.77E-13	6.43E-13
Mrk 332	27.3 ± 4.1	19.9	2.78E-13	3.67E-13	4.82E-13

|| The results of Mrk 993 are omitted from the analysis in this paper since the flux density at 200 μm from ISOPHOT for the galaxy may have a large calibration error (See section 3-2 in detail).